

Surface Assembly and Plasmonic Properties in Strongly Coupled Segmented Gold Nanorods

Maneesh K. Gupta, Tobias König, Rachel Near, Dhriti Nepal, Lawrence F. Drummy, Sushmita Biswas, Swati Naik, Richard A. Vaia, Mostafa A. El-Sayed, and Vladimir V. Tsukruk*

An assembly strategy is reported such that segmented nanorods fabricated through template-assisted methods can be robustly transferred and tethered to a pre-functionalized substrate with excellent uniformity over large surface areas. After embedding the rods, sacrificial nickel segments were selectively etched leaving behind strongly coupled segmented gold nanorods with gaps between rods below 40 nm and as small as 2 nm. Hyper-spectral imaging is utilized to measure Rayleigh scattering spectra from individual and coupled nanorod elements in contrast to common bulk measurements. This approach discerns the effects of not only changing segment and gap size but also the presence of characteristic defects on the plasmonic coupling between closely spaced nanorods. Polarized hyper-spectral measurements are conducted to provide direct observation of the anisotropic plasmonic resonance modes in individual and coupled nanorods, which are close to those predicted by computer simulations for nanorods with ideal shapes. Some common deviations from ideal shape such as non-flat facets and asymmetric tails are demonstrated to result in the appearance of characteristic plasmon resonances, which have not been considered before. The large-scale assembly of coupled noble nanostructures with fine control over geometry and high uniformity provides means to strongly tune the scattering, absorption, and near-field plasmonic properties through the geometric arrangement of precisely controlled nanorod segments.

M. K. Gupta, Dr. T. König, S. Naik, Prof. V. V. Tsukruk
School of Materials Science and Engineering
Georgia Institute of Technology Atlanta
GA 30332, USA

E-mail: vladimir@mse.gatech.edu

R. Near, Prof. M. A. El-Sayed
School of Chemistry and Biochemistry
Georgia Institute of Technology
Atlanta, GA 30332, USA

Dr. D. Nepal, Dr. L. F. Drummy, Dr. S. Biswas, Dr. R. A. Vaia
Materials and Manufacturing Directorate
Air Force Research Laboratory
Wright-Patterson AFB, OH 45433, USA

DOI: 10.1002/sml.201300248



1. Introduction

The coupling of localized surface plasmon resonances (LSPR) in noble metal nanostructures provides a versatile approach to precisely tailor optical properties such as absorption, scattering, and near-field enhancement.^[1–9] Recent studies have shown that nanoparticle assemblies with strongly coupled plasmons are of tremendous interest for a broad range of important applications including optoelectronics, photovoltaics, biological/chemical sensors, and nanophotonics to name a few.^[10–17] However, the ability to precisely fabricate large numbers of monodisperse assemblies remains a significant bottleneck for their effective utilization in many emerging applications.

Top-down fabrication techniques such as electron-beam lithography have been used with tremendous success to fabricate user-defined nanoparticle arrays. These tools have been widely used to study fundamental aspects of LSPR coupling interactions such as the ‘plasmon ruler equation’, and have more recently provided examples of Fano resonances and negative-index metamaterials in plasmonic systems.^[18–27] While these tools provide users with unparalleled control over the assembly geometry, they result in polycrystalline nanoparticles, which can have significant losses, and are largely restricted by the high-cost and intricacy of the fabrication process.^[28] On the other hand, bottom-up assembly of nanostructures, while offering advantages of single crystal structures, atomically smooth surfaces, low cost, and easy scalability, has typically been limited by the rigorous design requirements of chemical or biomolecular linkers needed to achieve diverse geometries and spacings along with the comparatively higher polydispersity among assemblies.^[29–38] However, recent studies have demonstrated tremendous progress in the efforts to generalize assembly of complex structures both in solution and on solid substrates.^[39–47]

Template based strategies have been shown to provide an intermediate approach for precisely fabricating plasmonic nanostructures with a high-degree of control and in large quantities relative to conventional top-down methods.^[48–52] In particular, porous anodic alumina (PAA) templates have proven to be extremely versatile for the fabrication of metal nanorods using both electro-less and electrodeposition methods.^[53–60] Based on these techniques a number of studies have demonstrated the ability to fabricate linear arrays of nanorods with controlled diameter, length, and gap between rod segments by sequential deposition of metals followed by selective etching of sacrificial metal segments.^[61–68] The strong near-field enhancement in the gaps between adjacent segments in these array structures have been thoroughly investigated especially for use in optical antenna and surface enhanced Raman scattering (SERS) applications.^[69–72] These template-assisted arrays have tremendous potential for a wide range of applications including photovoltaics, electronics, and biological/chemical sensing owing to the ability precisely tailor the geometric and compositional structure of the array along with the high-throughput and relatively low-cost of fabrication.

Current strategies for preserving the inter-rod gaps in template fabricated arrays are based on vapor phase deposition of backing layers followed by re-dispersion and then etching of sacrificial metal segments.^[73] This approach serves exceptionally well for applications, such as in situ biosensing, where dispersible nanorod arrays are desired.^[74] However, there remain numerous applications, including substrate-based sensors, photovoltaics, and optoelectronics, in which nanorod arrays are desired on fixed substrates. For these applications, high-throughput and efficient techniques to assemble these multi-segmented nanorods directly on substrates while preserving the local array structure are critical to realize the broader potential of these template-based arrays. Additionally, optical techniques capable of addressing and resolving individual array elements must be utilized to characterize the influence of structural, compositional, ambient dielectric, and

substrate interaction factors on the far-field optical properties. Currently measurement of far-field optical properties in template-assisted arrays has been limited to ensemble measurements of solutions of randomly oriented nanorods with unpolarized light.

In this report we develop materials processing strategies so that micron-long, multi-segmented nanorods with diameters as small as 50 nm, nanorod segments ranging from 70 to 150 nm in length, and gaps between nanorods ranging from 40 to 2 nm can be robustly transferred to a pre-functionalized substrate without compromising the original linear array structure. Hyper-spectral imaging was utilized to measure Rayleigh scattering spectra from the individual and coupled nanorod elements in contrast to common bulk measurements. This approach allowed us to discern the effects of not only changing segment and gap size but also the presence of characteristic defects on the plasmonic coupling between closely spaced nanorods. Polarized hyper-spectral measurements were conducted to provide direct observation of the anisotropic plasmonic resonance modes in individual and coupled nanorods which are close to those predicted by computer simulations for nanorods with ideal shapes. The polarized measurements also provided a means to identify scattering modes that may arise from anomalous structural features. Some common deviations from ideal shape such as non-flat facets and asymmetric tails were demonstrated to result in appearance of characteristic plasmon resonances which have not been considered before. Simulations of ideal and roughened nanorods allowed for identification of fine structural features that may cause the new scattering modes observed in polarized measurements of individual nanostructures.

2. Results and Discussion

2.1. Assembly of Segmented Nanorods on Surfaces

The linear nanorod arrays analyzed in this report were fabricated by sequential electrodeposition of silver, gold, and nickel metals into porous alumina templates with pore diameters of 50 nm (**Figure 1a–c**) using a thin sputter coated gold film as the working electrode (see Experimental Section). In order to facilitate high-throughput and monodisperse synthesis of the segmented nanorods, large area templates (>10 cm²) with highly uniform pore diameters were fabricated and used.

A major challenge of template-based fabrication is that upon dissolution of the template a significant number of the nanorods can become ‘bundled’ irreversibly into aggregates, significantly reducing the throughput of the synthesis. This problem is particularly severe with small diameter nanorods (<100 nm diameter) that have higher surface energy and a greater propensity to aggregate. To overcome these issues, we dissolved the alumina template in a 1M NaOH solution containing 10 mg/mL of polystyrene sulfonate (PSS) to act as a capping layer for the rods.^[75,76] Furthermore, the alumina was dissolved with the working electrode intact, and the rods were functionalized with PSS as an array. This approach kept the nanorods well separated allowing the PSS to diffuse

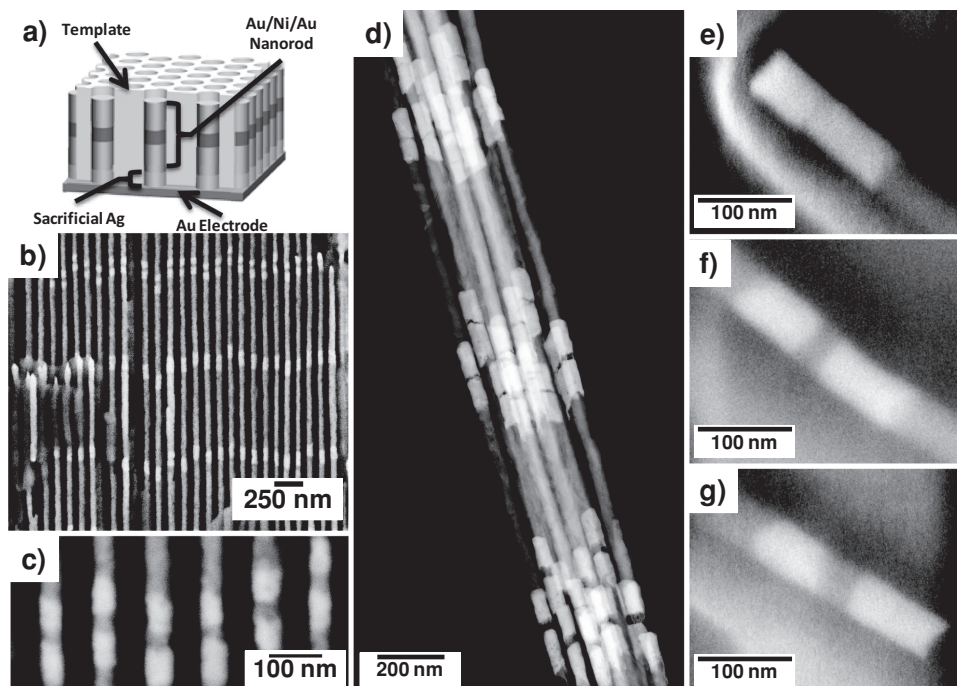


Figure 1. Segmented nanorods comprised of gold and nickel fabricated by electrodeposition in porous alumina templates. a) Schematic showing the segmented nanorods in the porous alumina template. b,c) Scanning electron microscopy (SEM) images of template cross section showing the segmented nanorods within the pores. The nanorods are comprised of gold and nickel segments with the gold appearing brighter. d) High angle annular dark field transmission electron microscopy (HAADF TEM) images of the nanorod dimers in array 1 with gap spacings of 15, 8 and 2 nm. e-g) SEM images of the nanorod dimers in array 2 with gap spacing of 40, 20, and 8 nm.

quickly and better coat the rods. After the template was dissolved and the rods were functionalized, they were dispersed and separated from the working electrode by selectively dissolving the sacrificial silver layer. We found that this strategy was effective at creating high-yield suspensions of nanorods that were well dispersed and remained so for several months.

The lengths of the metal segments in the nanorod arrays were controlled by varying the duration of the electrodeposition. In this way, we were able to reliably deposit metal layers as thin as 2 nm. For single particle scattering measurements, two different arrays of dimers were made. In the structure of array 1, the first nanorod was 70 nm long, followed by three sets of nanorod dimers with intra-dimer gaps of 15, 8, and 2 nm between 70 nm rods (Figure 1d), and finally a single nanorod 140 nm in length. In the second array (array 2), nanorod dimers with gaps of 40, 20, and 8 nm were fabricated (Figures 1e–g). The distance between adjacent rods or dimers was maintained to be at least 500 nm to minimize LSPR coupling interactions between the adjacent array elements.

In order to uniformly assemble the segmented nanorods directly on solid substrates while preserving the local array structure, two methods were developed. In the first method (method 1), the segmented nanorods suspended in ethanol were drop-cast on 70 nm thick polystyrene films at elevated temperature, allowing for immediate embedding of nanorods in the pre-melted polymer coating (Figure 2a). This routine is a critical step in the process that served several major purposes. First, at temperatures above the glass transition of the polystyrene (>110 °C) the deposited rods became partially embedded in the softened film and were frozen in place upon subsequent fast cooling. Second, this procedure immobilizes

the rods and allows selective etching of nickel segments in hydrochloric acid with preservation of the original array geometry and without disturbing the nanoscale dimensions of gaps between the rods (Figure 2b–e). Finally, the elevated temperature resulted in nearly instantaneous drying of the ethanol, and hence largely prevented capillary induced aggregation of the segmented rods, a common challenge for conventional drop-casting.

This method worked very well to firmly embed the nanorods and preserve the nanoscale gaps after etching the nickel segments. However, due to the transient nature of the deposition at high temperature, it was difficult to uniformly cover large area substrates with the segmented nanorods. Another challenge with this method was the difficulty in precisely controlling the distance between the rods and the substrate. With 70 nm thick polystyrene films, the rods were partially embedded in the polymer film and typically 20–30 nm above the substrate surface. In order to reduce this distance, we tried to embed the nanorods in thinner films. However, this led to dewetting of polymer films around the segmented rods and significant aggregation. Finally, while the polystyrene film was robust enough to withstand harsh aqueous solutions (38% aqueous HCl), exposure to organic solvents or high temperatures after removal of the nickel segments led to swelling or softening of the polymer film and significantly disrupted the array structure.

As a further improvement, we developed a second method (method 2) to immobilize the nanorod arrays allowing for more uniform coverage over larger areas and better control of the spacing between the nanorods and the substrate. This method was based upon electrostatic interactions between

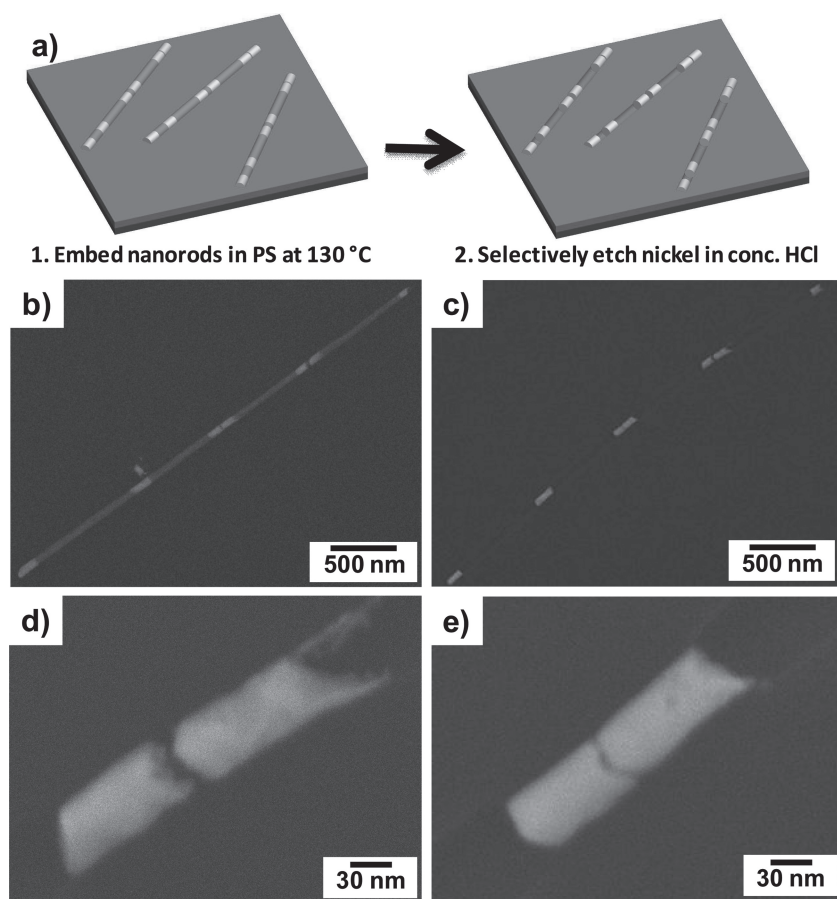


Figure 2. Assembly of segmented nanorods according to method 1. a) Schematic depicting the uniform assembly of nanorods. 1) The nanorods are firmly embedded in thin polystyrene films at high temperature ($>120\text{ }^{\circ}\text{C}$), 2) Selective etching of nickel segments to leave behind an array of gold dimers with precisely controlled gap size. b,c) SEM images of the nanorod arrays deposited by method 1 before and after nickel etching respectively. Images showing the full length of array 1 embedded in polystyrene. c,d) Higher-resolution images of nanorod dimers after nickel etching with 15 and 8 nm gaps between rods.

the negatively charged PSS coated nanorods and positively charged polyallylamine hydrochloride (PAH) functionalized substrates (**Figure 3**).^[77–79] Owing to the presence of the magnetic nickel segments, the nanorods could be magnetophoretically pulled from the suspension using a strong rare earth magnet placed below the substrate and fixed by electrostatic interactions between the oppositely charged polyelectrolytes (**Figure 3a**).^[80] This ensured that the deposition could be performed very quickly (<5 minutes) and that nearly all of the nanorods in suspension were deposited on the substrate. For the nanorods to remain rigidly fixed while etching the sacrificial metal layer, the polyelectrolytes used for immobilizing the nanorods must be carefully selected. As mentioned above, the nickel segments were etched using concentrated HCl solutions. So, to ensure that nanorods stay fixed the polyelectrolytes must remain charged at very low pH conditions and weak polyelectrolytes must be avoided. PSS/PAH served well for this reason as they did not dissociate or swell in a noticeable manner in the concentrated HCl solution during the 5 minute long etching step. SEM images show that the rods were rigidly bound and displayed excellent retention of

the gap structure and deposition concentration after etching of the nickel segments (**Figure 3b**).

The major advantage of method 2 is that it allowed for very uniform deposition of nanorods over large areas and with very high efficiency. The simple combination of magnetophoretic deposition and electrostatic interactions is particularly useful as it can be extended to a wide range of functionalized substrates. Layer-by-layer (LbL) techniques have proven to be extremely versatile at deposition of alternately charged polyelectrolytes on a wide range of substrates with varying surface chemistry, geometry, and topography. Furthermore, the nature of LbL techniques allows for precise control over the thickness of the polyelectrolyte layers. This control can allow the spacing between the nanorods and the substrate to be finely tuned, and ultimately provide a means to modulate potential interactions with the substrate. Finally, as long as the electrostatic interactions between the polyelectrolytes are maintained the assemblies are stable in a wide range of organic solvents and moderately high temperatures ($<200\text{ }^{\circ}\text{C}$).

2.2. Single Particle Scattering Measurements

Characterization of the far-field optical properties of substrate bound nanoparticles especially at the single particle level is particularly challenging. Conventional UV-Vis micro-spectrometry does

not typically allow for collection of spectra from individual array elements, as the collection areas are too large and result in spectra that are averaged over several array elements. In order to overcome the limitations of these conventional techniques, we utilized hyperspectral imaging in the dark-field mode, which allowed for recording of scattering spectra at wavelengths from 400–1000 nm at each pixel in a dark-field optical image. Optical pattern matching with SEM images was used to ensure that the scattering spectra were actually collected from single nanorod arrays and not bundles (**Figure 4**). Representative unpolarized spectra from each element in array 1 highlighted in **Figure 5a** along with the corresponding ensemble UV-Vis spectrum are shown in **Figure 5b**. As expected, the averaged spectrum for the entire linear array shows broad scattering from 550 to 900 nm with convoluted peaks due to the differential degree of coupling in each dimer.

The spectra for each individual particle or dimer in array 1 exhibit more distinct scattering peaks. The spectrum for the 70 nm rod shows transverse and longitudinal resonance modes at 550 and 675 nm respectively, in close agreement with

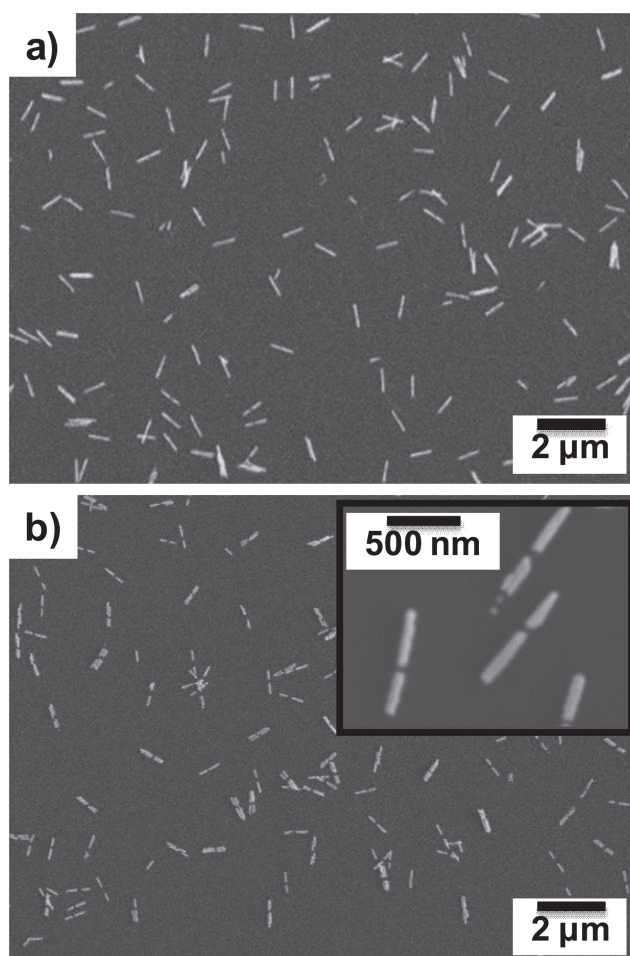


Figure 3. SEM images of nanorod dimers deposited by method 2 before and after nickel etching. a) Image showing well dispersed nanorods with relatively uniform coverage. b) The dimers remain adhered and maintain uniform coverage after etching the nickel segments. The inset image shows the consistent gap size between the dimers.

simulated spectra discussed in the next section. The spectra for the dimers with decreasing gap size exhibit a transverse mode consistent with the uncoupled nanorods at 550–570 nm. As expected, the longitudinal mode for these dimers indicates significant coupling effects by a strong increase in scattering at longer wavelengths.^[81] However, the spectra for the dimers and the 140 nm rod exhibit broad scattering with multiple convoluted peaks from 600 to 900 nm. We hypothesize that this broad scattering is caused by multi-pole resonance modes that may arise specifically due to roughness at the ends of the nanorods and appear more pronounced in strongly coupled or high aspect ratio nanorods. In order, to test this and more thoroughly resolve the coupling effects in dimers several follow-up experiments were performed.

First, a dimer array with larger gap spacing (array 2) was fabricated to determine if tunable coupling effects matching with simulated spectra could be clearly seen in systems with moderate coupling. Second, scattering spectra were collected again for array 1 with a polarized light source in an attempt to resolve anisotropic scattering modes in the strongly coupled dimers. Finally, the far-field optical properties of

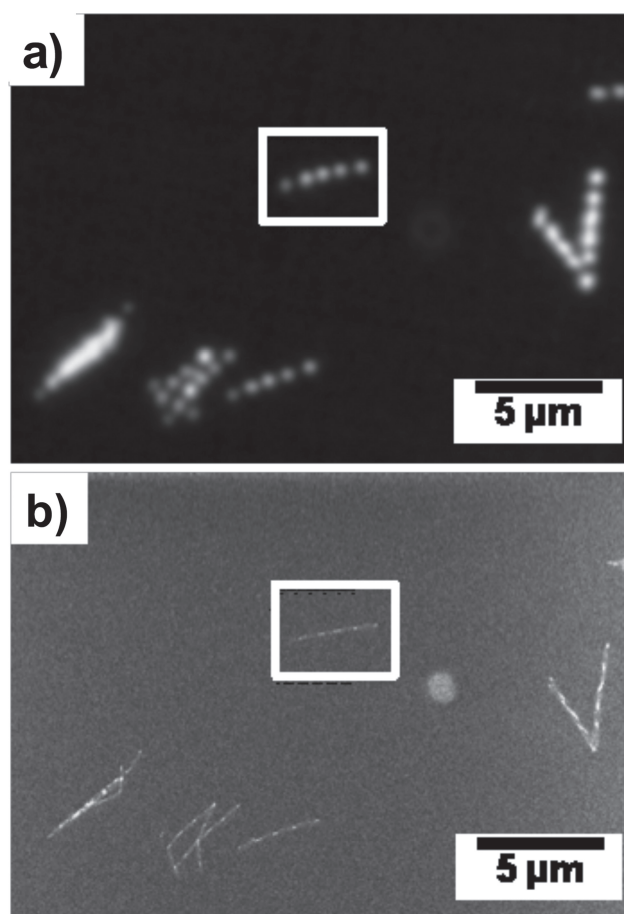


Figure 4. Optical pattern matching with SEM images was used to ensure that hyperspectral analysis was performed on single segmented nanorods. The nanorods in the a) hyperspectral dark-field image are clearly visible in the b) SEM image.

nanorods with specific non-flat end shapes routinely observed here were simulated in order to determine if specific modes observed in the experimental spectra could be attributed to these structural features.

The hyperspectral image of array 2 shows dimer arrays with 3 distinct spots each of a remarkably different color (Figure 5c) varying from green to red as the gap spacing decreases. This visible color shift is in stark contrast to the hyperspectral image of array 1 (Figure 5a) in which each array element appears a bright yellow color due to the broad scattering at long wavelengths. The corresponding spectra from array 2 (Figure 5d) clearly shows the longitudinal modes for each dimer pair shifting from 600 to 650 nm as the gap spacing decreased from 40 to 8 nm. Additionally, the spectra from array 2 do not show strong scattering beyond 700 nm in contrast to array 1 indicating overall weaker coupling, as expected, from the larger gaps sizes in the array structure. For comparison with the experimental results from array 2, spectra for the dimer pairs were simulated by the discrete-dipole approximation (DDA) method (Figure 5e). The simulated spectra exhibit a well-known red shift in the longitudinal mode as the spacing between nanorods is reduced. Figure 5f shows the relative change in peak position with gap size for the DDA calculations as well as arrays 1 and 2. For array 2, the relative shift for the

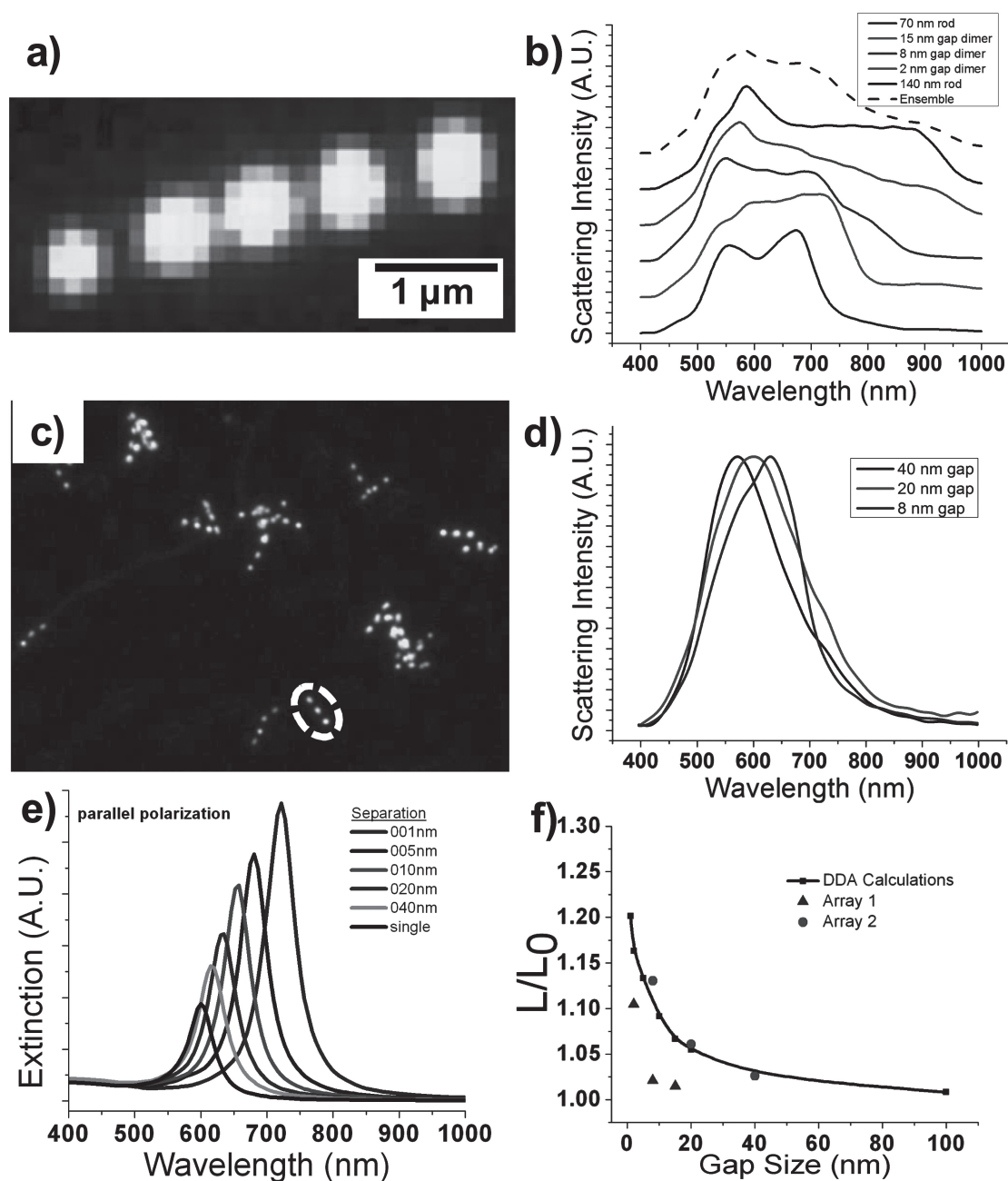


Figure 5. Hyperspectral dark-field images and unpolarized scattering spectra from arrays 1 and 2. a) High-resolution hyperspectral image of array 1. Each pixel in the image represents a scattering spectrum from 400 to 1000 nm. b) Scattering spectra corresponding to each dimer or rod shown in (a) along with integrated spectrum of a segmented nanorod (dashed line). c) Dark-field optical image of array 2 showing several arrays each consisting of 3 dimers each. d) Scattering spectra for dimers in array 2 with decreasing gap size resulting in a noticeable red-shift in the longitudinal mode. e) DDA simulations of nanorod dimers showing the expected shift in the longitudinal mode. f) Comparison of the magnitude of the shift in the longitudinal mode with decreasing gap size, showing good correlation between the experimental and simulated results.

longitudinal mode was calculated using 570 nm as the position for the uncoupled longitudinal mode. The absolute peak positions, however, were slightly red shifted from the experimental results, which may result from small discrepancies between the simulated and experimental systems. Indeed, the simulations were performed for perfectly cylindrical dimers in uniform medium with average refractive index of 1.53. Whereas, the experiments were performed with dimers having rough ends

and at the interface between the polystyrene film with refractive index of 1.55 and the immersion oil with refractive index of 1.515.

The results from array 2 indicate that the expected shifts in the longitudinal mode due to coupling can be observed in moderately coupled dimers without giving rise to broad scattering at longer wavelengths. However, in order to more clearly resolve the spectra from the strongly coupled

dimers in array 1, we performed high-resolution hyper-spectral imaging with a polarized light source. The spectra collected for the individual nanorods and dimers clearly reveal the anisotropic nature of the optical scattering modes, which was not observed in the unpolarized measurements. The scattering spectra at different polarization angles for all elements in array 1 are shown in **Figure 6a** with 0 and 180 degrees corresponding to the long axis of the nanorod array. The relative intensities of the plasmon

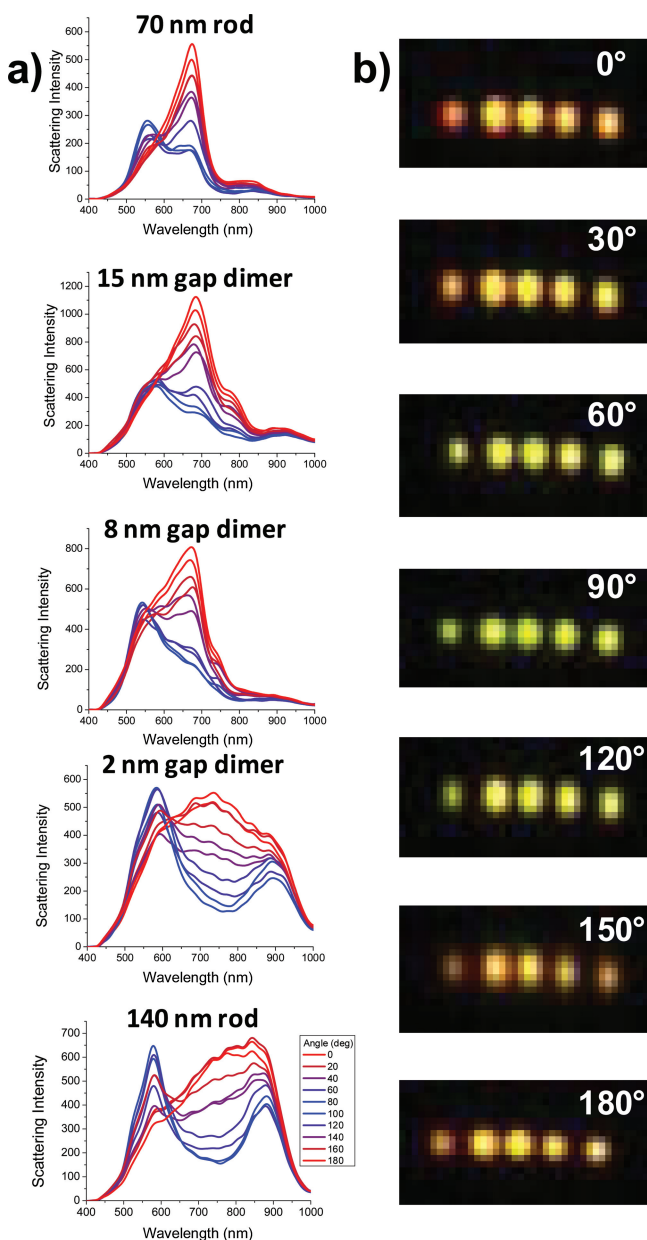


Figure 6. a) Polarized scattering for each dimer or rod in array 1. 0 and 180 degrees polarization correspond to the long axis of the dimer array (red lines), and 90 degrees polarization is perpendicular to the long axis of the dimer array (blue lines). Polarized spectra show selective excitation of the transverse and longitudinal modes with varying polarization angle. b) Dark-field optical images collected with polarized incoming light. The images show change in the predominant scattering mode from a red/orange color corresponding to the longitudinal mode excited at 0 and 180 degrees, to a green color corresponding to the transverse mode excited at 90 degrees.

peaks vary dramatically with polarization orientation. At 0 and 180 degrees relative to the long axis of the linear array, the electric field component of the incident light is primarily in the long axis of the rod, and as a result the longitudinal modes are preferentially excited. Conversely, at 90 degree orientation the transverse mode is primarily excited.^[82,83]

The spectra collected for the single 70 nm rod shows selective excitation of both the transverse and longitudinal plasmon modes at 550 nm and 675 nm, respectively. For all other array elements, the position of the transverse mode stays within 550 to 580 nm close to that of the uncoupled 70 nm rod. In the 15 and 8 nm gap dimers, the longitudinal mode appears at 700 nm and is red-shifted compared to the uncoupled nanorod. The polarized measurements were critical to identify the longitudinal mode for the 2 nm gap dimer and the 140 nm rod. In both cases, an additional peak appears at 900 nm, which caused the peaks in the unpolarized spectra to appear broad and convoluted. However, in the polarized spectra the longitudinal mode becomes visible due to its modulation with polarization angle and appears at 750 and 775 nm, respectively. The ability to perform these polarized measurements at the single particle/dimer level provided a means to separate and identify the expected resonance modes.^[81]

The polarization dependence of the plasmon excitation is also directly visible from the dark-field optical images that were collected at different polarization angles (Figure 6b). The first spot in the linear array (from the left side) is the terminal gold rod of 70 nm length. The light scattered by this particle shifts from red at 0 degrees, to green at 90 degrees, and back to red at 180 degrees. This agrees well with selective excitation of the red longitudinal mode and green transverse mode at the corresponding angles. Similar trends are observed for other segments, however, with some orange/yellow color at 0 and 180 due to scattering at longer wavelength, which may be compromised by the limited detector sensitivity for wavelengths above 900 nm.

The polar charts in **Figure 7** show the angular variation for the relative intensities of the transverse and longitudinal modes for each segment of array 1. The angular variation of the scattering intensity data, $I(\theta)$, were fitted by phase-shifted sine squared functions, as predicted for gold nanorods, in the form:^[84]

$$I(\theta) = \alpha_{\perp} \sin^2(\theta - \theta_{\perp}) + \alpha_{\parallel} \cos^2(\theta - \theta_{\parallel})$$

where α_{\parallel} and α_{\perp} are polarization anisotropy ratio for the longitudinal and transverse bands, respectively and θ is the polarization angle.

For the 70 nm gold rod, the maximum for longitudinal mode is achieved at $\theta = 0.7 \pm 1.5^\circ$, and $\theta = 92.4 \pm 1.5^\circ$ for transverse mode, very close to the expected values. The half-widths of polarization dependencies are close to 50° for both modes. Anisotropy ratios were 5 for longitudinal LSPR modes and decreased to 2 for transverse mode. According to recent theoretical estimations, for purely dipolar behavior the polarization anisotropy ratio can reach 10-100 for extinction of the longitudinal mode. The reduction of the polarization

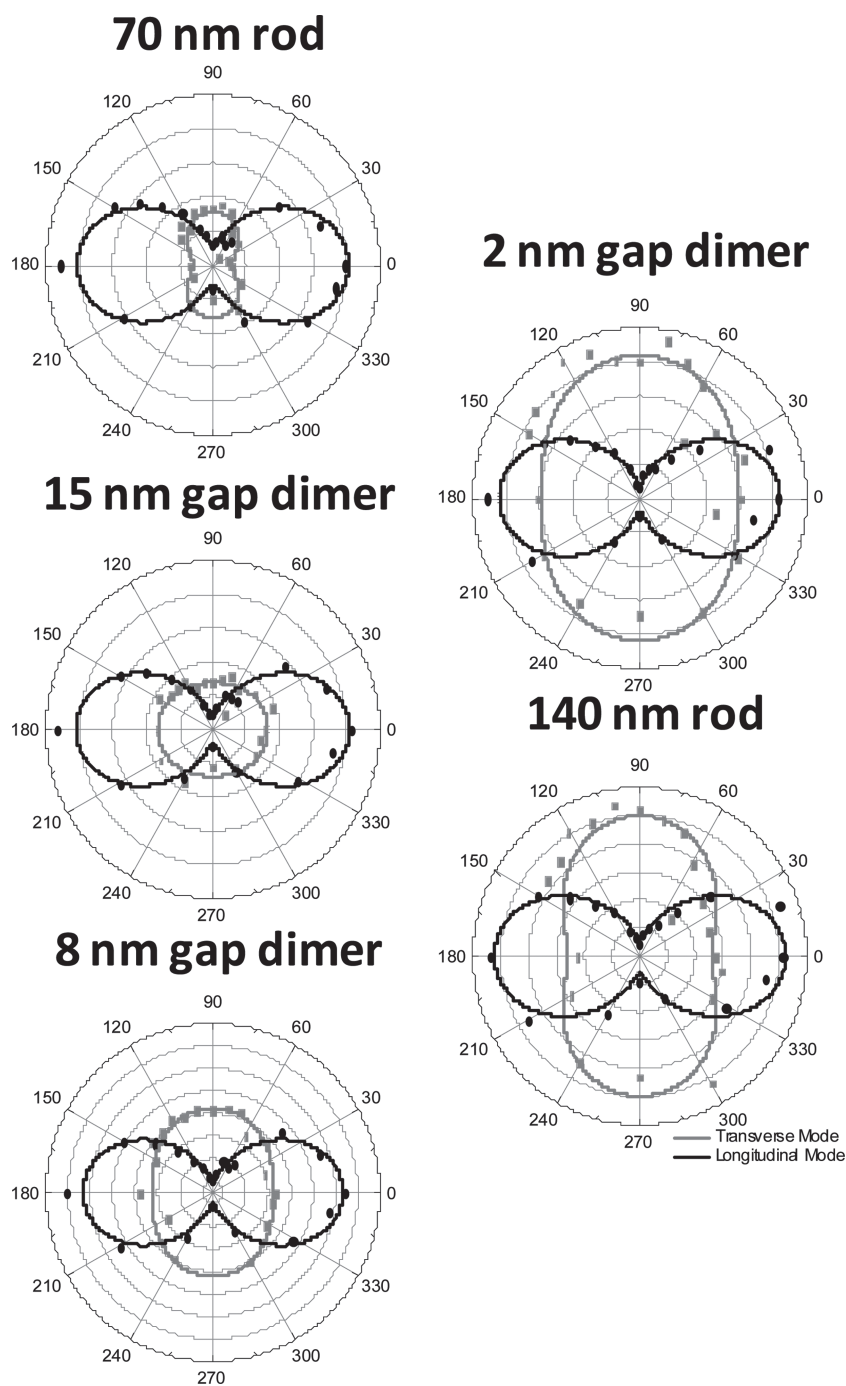


Figure 7. Polar charts showing the relative intensities of the transverse (pale lines) and longitudinal (dark lines) modes for each dimer or rod in array 1.

anisotropy to 5 observed here for scattering intensity can be related to several factors. Firstly, the gold nanorods fabricated had a relatively low aspect ratio of approximately 1.4, which is considerably smaller than typically aspect ratio reported earlier (>2) and inherently leads to weaker polarization anisotropy. Secondly, the polarization anisotropy can be weakened by inhomogeneous broadening of the longitudinal mode. Considering that we conducted spectral measurements for individual nanorod dimers in contrast to conventional bulk measurements, the last factor cannot be related to this

nanostructure inhomogeneity but rather with roughness at the gold nanorod ends as will be addressed in simulations discussed below.^[85–87]

It is worth noting that, apart from the expected transverse and longitudinal dipolar modes, a few other unique features have been detected in the polarized spectra of individual nanorods. Indeed, in the spectra for the 70 nm rod, a small peak appears at 833 nm. This peak seems to shift to 900 nm for the remaining elements, and dramatically intensifies for the 2 nm gap dimer and the 140 nm rod. The longitudinal mode for both the 15 and 8 nm gap dimers contain a red-shifted shoulder peak, and the transverse mode for the 15 and 2 nm gap dimers and the 140 nm rod contain a blue-shifted shoulder peak. The presence of the consistent SPR peaks usually indicates the presence of nanostructural elements with different transversal or longitudinal dimensions. However, in our case this explanation is not supported by direct high-resolution observation of large nanorod arrays which shows very uniform (within 5%) geometrical dimensions of all segments fabricated here.

Therefore, in order to understand the potential contribution of the roughness at the ends of the nanorods towards these scattering modes, finite-difference time-domain (FDTD) simulations were performed for real nanorod shapes with varying end geometry (actual defects). From SEM images, we found that the ends of the nanorods commonly deviated from a flat geometry and often have a concave or convex curvature at their tips as well as asymmetric end shape with sharp ‘tails’. For example, in Figure 2e the rod ends on either side of the gap show this morphology clearly. Another feature that was routinely observed was “comet-tail” like morphology that extent from the ends of some rods (shown in the top right nanorod in Figure 2d).

The effects of deviations of these end shapes from ideal flat facets were simulated for 70 nm long uncoupled nanorods asymmetric shapes to be simulated by different combinations of convex and concave shapes of different facets. The resulting simulated spectra for different scenarios are shown in **Figure 8**. The peak positions for the transverse and longitudinal modes in the simulated spectra to differ significantly from that for the ideal shape. These shifted positions were found to match well with the experimentally measured results (555 and 673 nm, respectively).

Different combinations of non-flat facets might result in very different scenarios for SPR peaks shifts. The first three

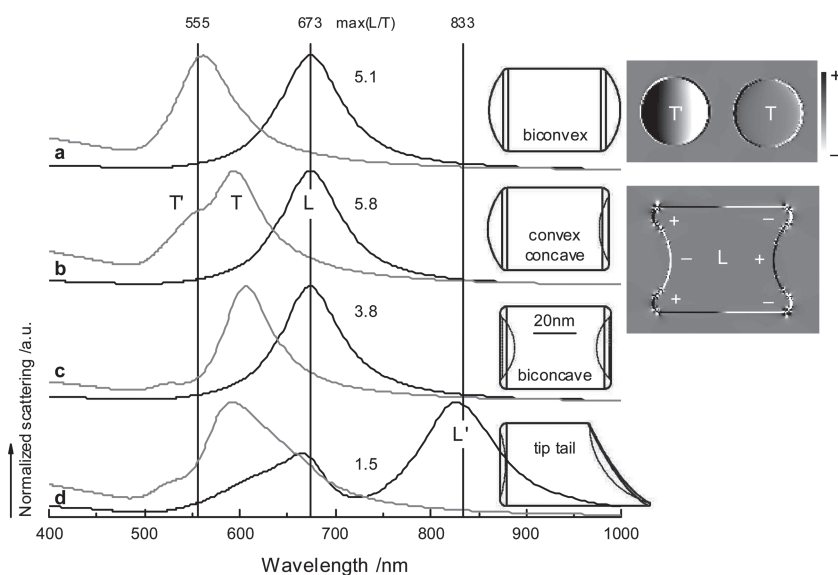


Figure 8. FDTD simulations of the effects of the tip shape on the scattering modes in uncoupled gold nanorods. a-c) Simulated spectra for nanorods with a combination of convex or concave tip shapes. Nanorods with concave tip shapes show a second transverse mode at higher energy, which was also observed in the experimental results. d) Simulated spectrum for a nanorod with a 'comet-tail'-like tip which resulted in a new peak appearing at 830 nm.

rods shown (Figure 8a-c) contain different combinations of the convex and concave end shapes. Interestingly, in the cases where a concave end is present we observed splitting of the transverse mode (Figure 8b,c). The charge plots shown in the upper left inset indicate that this new transverse mode (T') is the second order resonant mode and as result appears at a higher energy. In the case of a biconcave tip shape the charges are symmetric distributed correspondingly to the symmetry of the nanorod. The position of this higher order transverse mode agrees well with the experimental spectra where a blue-shifted shoulder peak was observed for the 15 and 2 nm gap dimers and 140 nm rod.

Finally, Figure 8d shows the simulated spectra for a peculiar nanorod with the 'comet-tail' morphology on one side which is also frequently observed in the nanorods. Such a highly asymmetric nanorod shape resulted in a large resonance peak appearing at longer wavelength around 830 nm that is close to the additional surprising peak observed for the 70 nm nanorods.

Our simulations showed that an asymmetric tip tail generated by sphere (or etched by sphere) with the radius of 100 nm results in an additional longitudinal mode (L') (Figure 9). Experimentally, a ratio of maximum of longitudinal scaled by the maximum of the transverse mode was measured of 1.78 (max(L/T)). In all cases the longitudinal mode wavelength could be achieved by adjusting the length of the nanorod. Change in the tip shape results in altering of the LSPR mode shown by the surface charges distributions. The second transverse mode (T') could be identified as

an additional inverted charge at the outer shell compare to the transverse mode (T). The tip tail alters the symmetrical charge distribution for ideal symmetrical nanorods significantly with results of two longitudinal modes (Figure 9). The 672 nm mode (L) is similar to a biconcave mode. The second longitudinal mode shows a higher amount of charge separation with a charge concentration in the tip tail. This higher amount of charge separation is responsible for the higher intensity at the L'-mode which is different from the experimental observations. This discrepancy can be related to mismatch of the orientation between longitudinal polarization and the long axes of the nanorod during measurements which can easily be within $\pm 10^\circ$.

3. Conclusion

The inherent advantage of the template based strategy employed here is the ability to generate tailored linear arrays of rods with fine control over rod diameter, length, and spacing between rods. In this report, we have extended the versatility of this approach by demonstrating a simple method to transfer these linear nanorod assemblies in high quantity onto surfaces while preserving the fidelity of the local array structure. Moreover, we were able to measure the highly anisotropic LSPR optical properties at the single particle level using high-resolution hyperspectral imaging and suggest the origin of the multiple plasmon resonances including some peculiar optical features caused by characteristic fabrication defects. This capability to fabricate programmable assemblies and measure optical properties at the single particle level will be crucial for the practical development of plasmonic antennas, SERS sensors, and multiplexed biological/chemical LSPR sensors. Future efforts must be undertaken to understand the effects of roughness at the rod ends on the optical

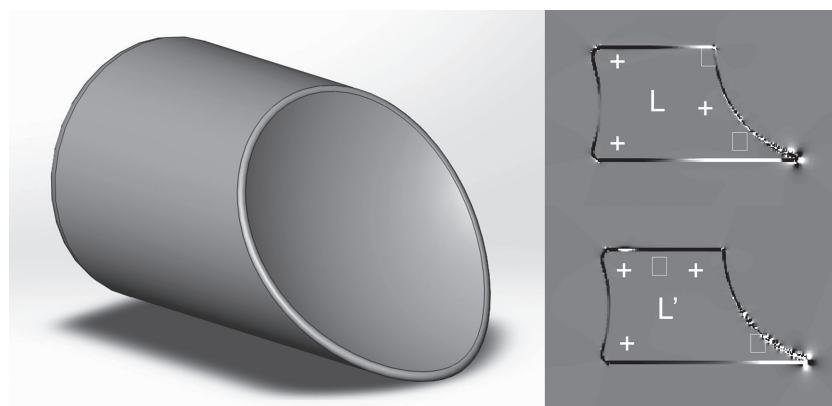


Figure 9. FDTD simulations of the effects of the end tip shape on the scattering modes: 3D model of asymmetric tail along with plots of two strongest asymmetric charge distribution modes which contribute to the appearance of new long-wavelength resonance.

properties of template fabricated nanorods, especially in the regime of strong LSPR coupling. With further improvement in the assembly of these segmented nanorods with long-range order, this strategy has strong potential towards practical applications.

4. Experimental Section

All aqueous solutions were prepared using 18.2 M Ω cm water obtained from a Barnstead Nanopure-UV system. Porous anodic alumina (PAA) templates were fabricated by anodization of 99.999% purity aluminum foils (as-rolled, 1 mm thickness from Goodfellow Corporation). The foil was cut into 3 cm x 4 cm coupons and degreased first in acetone and then ethanol. A Keithley 2400 power supply was used to supply current and voltage for electropolishing and anodization steps. Coupons were electropolished in a solution comprised of 100 ml 60% perchloric acid solution (Alfa Aesar) and 400 ml 99.9% ethanol (*Caution: vapor from perchloric acid can form explosive crystals!*) at 7 °C by passing 1 A of current at 20 V for 15 min.^[88] The coupons were then extensively rinsed in ethanol and dried in a nitrogen stream. Before anodization, one side of the coupons was protected with Tolber Miccro XP-2000 stop-off paint to prevent current leakage.

Anodization was performed in two stages using an aqueous 0.3 M oxalic acid (Alfa Aesar) solution at 15 °C and 40 V. The first anodization was carried out for 15 h to create well-ordered vertically oriented pores. After the first anodization, the oxide layer was completely etched in a chromic acid solution (1.8 wt% CrO₃ and 3.5 wt% H₃PO₄) at 65 °C for 2 h. The second anodization was carried out for 6 hours to achieve the desired membrane thickness of 40 micrometers. The pore side of the membrane was protected by spin coating a layer of cellulose acetate from a 3 wt% solution in acetone. The remaining back side aluminum was removed in a solution of 6 g CuCl₂ in 75 mL 38% HCl and 75 ml water. After completely removing the aluminum, the bottom side of the pores (adjacent to the aluminum) was opened in a 1 M NaOH solution for 2 min to yield through-hole pores. Finally, the protective cellulose acetate layer was dissolved in acetone, and the membrane was extensively rinsed in water and allowed to air dry.

Metal deposition was started by sputtering a 50 nm thick gold layer on the PAA template to serve as the working electrode and attached at the edge to a thin wire using conductive silver paste. A thick sacrificial nickel layer was then deposited from a commercial nickel sulfamate RTU solution (Technic Inc) by applying a -1.8 V potential using a Keithley 2400 sourcemeter for 10 min. This thick nickel layer served to seal the pores, allowing deposition to only occur inside the pores in the next step. The membrane was then mounted in a custom made Teflon electrochemical cell with only the open side of the pores exposed to the electrolyte. Sequential nickel and gold depositions were carried out using commercial solutions from Technic as described above for nickel and Orotemp 24 RTU for gold. Depositions were performed at -0.9 V with respect to a saturated calomel reference electrode. A thin platinum foil was used as the counter electrode and potential was applied using a Gamry series G potentiostat. The total charge deposited was measured real-time by the potentiostat and monitored to control the lengths of the individual segments. The cell was thoroughly rinsed in between segments to remove any residual electrolyte.

After deposition, the wires were removed by first dissolving the PAA template in 1 M NaOH containing 10 mg/mL PSS. Typically, a quarter of the sample area (~1.25 cm²) was dissolved in 1.5 mL of KOH/CTAB solution. The segmented rods were purified by repeated centrifugation and rinsing. A total of 8 rinses were used: the initial 5 rinses were performed with 30 mg/mL CTAB solution to remove residual salt, next two rinses with water to remove excess CTAB, and finally rods were rinsed and dispersed in ethanol.

PS films were spin cast on freshly piranha cleaned glass or silicon substrates using a 1 wt% solution of 250,000 MW PS in toluene at 3000 rpm. The PS coated substrates were then placed on a hotplate at 150 °C and were allowed to equilibrate for 5-10 min. The segmented rod ethanol dispersion was then deposited dropwise on the heated substrates to embed the rods in the PS layer. Once embedded, the nickel segments were etched in 38% HCl for 1-2 min with extensive rinsing in water afterwards to remove any residue.

SEM images were collected using a Zeiss Ultra 60 FE-SEM and a Hitachi S-3400 SEM with accelerating voltage typically at 5–10 kV and working distance of 5-7 mm. Dark-field imaging (100 \times) of gold nanorods was done using an Olympus BX-51 microscope and 100 W quartz halogen light source on a CytoViva microscope and software. Spectral data were captured with a CytoViva spectrophotometer and integrated CCD camera. Each spectrum shown represents a single pixel imaged with a 100 \times objective and approximately 64 nm in size. Samples were prepared on glass slides to allow scattering measurements to be performed in transmission mode. The sample was covered with type A immersion oil and then covered with a cover slip and sealed with nail polish to minimize disturbances. Each spectra is normalized by dividing it by a reference region (identical width, but with no particles). Spectral analysis was performed with the CytoViva Hyperspectral analysis software (ENVI) program. For polarized dark-field scattering measurements, the incident light was polarized with a linear polarizer. The direction of polarization was rotated between 0–360°.

High Angle Annular Dark Field-Scanning Transmission Electron Microscopy (HAADF-STEM) was performed on a 300 kV Cs-corrected FEI Titan. Spot size 9, a convergence angle of 7.2 mrad, and an annular detector camera length of 105 mm, and a Fischione model 3000 PMT detector were used to collect the images.

The optical response of gold nanorods with varying interparticle separation was calculated using the DDA method with the DDSCAT 6.1 code offered publicly by Draine and Flatau. The dielectric values for gold reported by Johnson and Christy were used and the medium surrounding the particle was represented as oil with a refractive index of 1.51. For calculation of the scattering spectra and the surface charges distributions, we used the commercial software from Lumerical Solutions Inc. (FDTD Solutions, Version 7.5.7). The nanorod models were designed in SolidWorks (Education Edition, 2012 SP 3.0). The data were saved in the STereoLithography (STL) format and afterwards converted into a Lumerical Solutions Inc. readable file format called Graphic Database System (GDSII) format via STL2GDS from Artwork Conversion (Version 1.24). According to the GDSII data format the nanorods were sliced in 1 or 0.5nm thickness (corresponding to simulation mesh), respectively. Longitudinal and transversal modes were simulated by the corresponding polarization.

Simulations with an edge rounding of 4nm of the concave tip face were set to 1nm mesh size. Mesh size of the tip tail was set

to 0.5 nm for best possible rendering of the edges. First conformal variant was used for mesh refinement. The mesh size was stretched above the whole field source with the following x-y-z-dimensions: 200, 150 and 150 nm (x-axes correspond to the longitudinal axes). All simulations were well converged below the simulation time of 75 fs at an auto shutoff level of 10^{-5} . As boundary conditions perfect match layer (PML) was used. The gold permittivity was chosen from Johnson and Christy^[89] and fitted by a 8 coefficient function showing an RMS error of 0.206 at a fitting range between 400 and 1000 nm. The background index was chosen over the mentioned spectra according to the experimentally used oil index (1.515).^[90,91]

Acknowledgements

We would like to thank for support the FA9550-11-1-0233 and FA9550-09-1-0162 (BIONIC Center) from Air Force Office of Scientific Research and Air Force Research Lab. We acknowledge J. Deneault and Dr. M. Durstock for help in preparation of porous anodic alumina templates.

- [1] N. J. Halas, S. Lal, W. S. Chang, S. Link, P. Nordlander, *Chem. Rev.* **2011**, *111*, 3913.
- [2] R. Elghanian, J. J. Storhoff, R. C. Mucic, R. L. Letsinger, C. A. Mirkin, *Science* **1997**, *277*, 1078.
- [3] S. Nie, S. R. Emory, *Science* **1997**, *275*, 1102.
- [4] M. K. Gupta, S. Chang, S. Singamaneni, L. F. Drummy, R. Gunawidjaja, R. R. Naik, V. V. Tsukruk, *Small* **2011**, *7*, 1192.
- [5] S. Chang, H. Ko, R. Gunawidjaja, V. V. Tsukruk, *J. Phys. Chem. C* **2011**, *115*, 4387.
- [6] A. M. Funston, C. Novo, T. J. Davis, P. Mulvaney, *Nano Lett.* **2009**, *9*, 1651.
- [7] B. Willingham, D. W. Brandl, P. Nordlander, *Appl. Phys. B* **2008**, *93*, 209.
- [8] K. C. Woo, L. Shao, H. Chen, Y. Ling, J. Wang, H.-Q. Lin, *ACS Nano* **2011**, *5*, 5976.
- [9] P. K. Jain, M. A. El-Sayed, *J. Phys. Chem. C* **2008**, *112*, 4954.
- [10] J. A. Schuller, E. S. Barnard, W. Cai, Y. C. Jun, J. S. White, M. L. Brongersma, *Nat. Mater.* **2010**, *9*, 193.
- [11] H. A. Atwater, A. Polman, *Nat. Mater.* **2010**, *9*, 205.
- [12] J. N. Anker, W. Paige Hall, O. Lyandres, N. C. Shah, J. Zhao, R. P. Van Duyne, *Nat. Mater.* **2008**, *7*, 442.
- [13] R. A. Alvarez-Puebla, L. M. Liz-Marzan, *Small* **2010**, *6*, 604.
- [14] H. Ko, S. Singamaneni, V. V. Tsukruk, *Small* **2008**, *4*, 1576.
- [15] R. Gunawidjaja, S. Peleshanko, H. Ko, V. V. Tsukruk, *Adv. Mater.* **2008**, *20*, 1544.
- [16] H. Ko, S. Chang, V. V. Tsukruk, *ACS Nano* **2009**, *3*, 181.
- [17] S. Chang, H. Ko, S. Singamaneni, R. Gunawidjaja, V. V. Tsukruk, *Anal. Chem.* **2009**, *81*, 5740.
- [18] W. Rechberger, A. Hohenau, A. Leitner, J. R. Krenn, B. Lamprecht, F. R. Aussenegg, *Opt. Commun.* **2003**, *220*, 137.
- [19] P. K. Jain, W. Huang, M. A. El-Sayed, *Nano Lett.* **2007**, *7*, 2080.
- [20] P. K. Jain, M. A. El-Sayed, *Chem. Phys. Lett.* **2010**, *487*, 153.
- [21] C. Tabor, D. Van Haute, M. A. El-Sayed, *ACS Nano* **2009**, *3*, 3670.
- [22] R. Near, C. Tabor, J. Duan, R. Pachter, M. A. El-Sayed, *Nano Lett.* **2012**, *12*, 2158.
- [23] V. M. Shalaev, W. Cai, U. K. Chettiar, H. K. Yuan, A. K. Sarychev, V. P. Drachev, A. V. Kildishev, *Opt. Lett.* **2005**, *30*, 3356.
- [24] J. B. Lassiter, H. Sobhani, J. A. Fan, J. Kundu, F. Capasso, P. Nordlander, N. J. Halas, *Nano Lett.* **2010**, *10*, 3184.
- [25] Z. Fang, J. Cai, Z. Yan, P. Nordlander, N. J. Halas, X. Zhu, *Nano Lett.* **2011**, *11*, 4475.
- [26] J. Ye, F. Wen, H. Sobhani, J. B. Lassiter, P. Van Dorpe, P. Nordlander, N. J. Halas, *Nano Lett.* **2012**, *12*, 1660.
- [27] B. Luk'yanchuk, N. I. Zheludev, S. A. Maier, N. J. Halas, P. Nordlander, H. Giessen, C. T. Chong, *Nat. Mater.* **2010**, *9*, 707.
- [28] P. Nagpal, N. C. Linkquist, S.-H. Oh, D. J. Norris, *Science* **2009**, *325*, 594.
- [29] K. Kiu, Z. Nie, N. Zhao, W. Li, M. Rubinstein, E. Kumacheva, *Science* **2010**, *329*, 197.
- [30] Z. Nie, D. Fava, M. Rubinstein, E. Kumacheva, *J. Am. Chem. Soc.* **2008**, *130*, 3683.
- [31] A. P. Alivisatos, K. P. Johnsson, X. Peng, T. E. Wilson, C. J. Loweth, M. P. Bruchez, P. G. Schultz, *Nature* **1996**, *382*, 609.
- [32] S. Y. Park, A. K. R. Lytton-Jean, B. Lee, S. Weigand, G. C. Schatz, C. A. Mirkin, *Nature* **2008**, *451*, 553.
- [33] D. Nykpanchuk, M. M. Maye, D. van der Lelie, O. Gang, *Nature* **2008**, *451*, 549.
- [34] A. Guerrero-Martinez, J. Perez-Juste, E. Carbo-Argibay, G. Tardajos, L. M. Liz-Marzan, *Angew. Chem. Int. Ed.* **2009**, *48*, 9484.
- [35] S. Pal, Z. Deng, H. Wang, S. Zou, Y. Liu, H. Yan, *J. Am. Chem. Soc.* **2011**, *133*, 1706.
- [36] J. M. Slocik, F. Tam, N. J. Halas, R. R. Naik, *Nano Lett.* **2007**, *7*, 1054.
- [37] M. P. Busson, B. Rolly, B. Stout, N. Bonod, E. Larquet, A. Polman, S. Bidault, *Nano Lett.* **2011**, *11*, 5060.
- [38] M. Rycenga, J. M. McLellan, Y. Xia, *Adv. Mater.* **2008**, *20*, 2416.
- [39] D. Nepal, K. Park, R. A. Vaia, *Small* **2012**, *8*, 1013.
- [40] N. Gandra, A. Abbas, L. Tian, S. Singamaneni, *Nano Lett.* **2012**, *12*, 2645.
- [41] R. J. Macfarlane, B. Lee, M. R. Jones, N. Harris, G. C. Schatz, C. A. Mirkin, *Science* **2011**, *334*, 204.
- [42] K. Park, H. Koerner, R. A. Vaia, *Nano Lett.* **2010**, *10*, 1433.
- [43] D. Nepal, M. S. Onses, K. Park, M. Jespersen, C. J. Thode, P. F. Nealey, R. A. Vaia, *ACS Nano* **2012**, *6*, 5693.
- [44] C. Kuemin, L. Nowack, L. Bozano, N. D. Spencer, H. Wolf, *Adv. Funct. Mater.* **2012**, *22*, 702.
- [45] T. Thai, Y. Zheng, S. H. Ng, S. Mudie, M. Altissimo, U. Bach, *Angew. Chem. Int. Ed.* **2012**, *51*, 8732.
- [46] Z. Sun, W. Ni, Z. Yang, X. Kou, L. Li, J. Wang, *Small* **2008**, *4*, 1287.
- [47] S. Chang, S. Singamaneni, E. Kharlampieva, S. L. Young, V. V. Tsukruk, *Macromolecules* **2009**, *42*, 5781.
- [48] C. R. Martin, *Science* **1994**, *266*, 1961.
- [49] M. R. Jones, K. D. Osberg, R. J. Macfarlane, M. R. Langille, C. A. Mirkin, *Chem. Rev.* **2011**, *111*, 3736.
- [50] S. J. Hurst, E. K. Payne, L. Qin, C. A. Mirkin, *Angew. Chem. Int. Ed.* **2006**, *45*, 2672.
- [51] T. R. Kline, M. Tian, J. Wang, A. Sen, M. W. H. Chan, T. E. Mallouk, *Inorg. Chem.* **2006**, *45*, 7555.
- [52] L. Jiang, Y. Sun, F. Huo, H. Zhang, L. Qin, S. Li, X. Chen, *Nanoscale* **2012**, *4*, 66.
- [53] D. AlMawlawi, N. Coombs, M. Moskovits, *J. Appl. Phys.* **1991**, *70*, 4421.
- [54] S. R. Nicewarner-Pena, R. G. Freeman, B. D. Reiss, L. He, D. J. Pena, I. D. Walton, R. Cromer, C. D. Keating, M. J. Natan, *Science* **2001**, *294*, 137.
- [55] R. Elnathan, R. Kantaev, F. Patolsky, *Nano Lett.* **2008**, *8*, 3964.
- [56] W. Lee, R. Scholz, K. Nielsch, U. Gosele, *Angew. Chem. Int. Ed.* **2005**, *44*, 6050.
- [57] C. D. Keating, M. J. Natan, *Adv. Mater.* **2003**, *15*, 451.
- [58] S. Kim, K. L. Shuford, H.-M. Bok, S. K. Kim, S. Park, *Nano Lett.* **2008**, *8*, 800.
- [59] S. Kim, S. K. Kim, S. Park, *J. Am. Chem. Soc.* **2009**, *131*, 8380.
- [60] A. L. Schmucker, N. Harris, M. J. Banholzer, M. G. Blaber, K. D. Osberg, G. C. Schatz, C. A. Mirkin, *ACS Nano* **2010**, *4*, 5453.
- [61] S. Liu, J. B.-H. Tok, Z. Bao, *Nano Lett.* **2005**, *5*, 1071.
- [62] L. Qin, S. Park, L. Huang, C. A. Mirkin, *Science* **2005**, *309*, 113.

- [63] T. Mirkovic, M. L. Foo, A. C. Arsenault, S. Fournier-Bidoz, N. S. Zacharia, G. A. Ozin, *Nat. Nanotech.* **2007**, *2*, 565.
- [64] K. D. Osberg, A. L. Schmucker, A. J. Senesi, C. A. Mirkin, *Nano Lett.* **2011**, *11*, 820.
- [65] L. Qin, J.-W. Jang, L. Huang, C. A. Mirkin, *Small* **2007**, *3*, 86.
- [66] L. Qin, M. J. Banholzer, J. E. Millstone, C. A. Mirkin, *Nano Lett.* **2007**, *7*, 3849.
- [67] M. J. Banholzer, K. D. Osberg, S. Li, B. F. Mangelson, G. C. Schatz, C. A. Mirkin, *ACS Nano* **2010**, *4*, 5446.
- [68] W. Wei, S. Z. Li, L. D. Qin, C. Xue, J. E. Millstone, X. Y. Xu, G. C. Schatz, C. A. Mirkin, *Nano Lett.* **2008**, *8*, 3446.
- [69] L. Qin, S. Zou, C. Xue, A. Atkinson, G. C. Schatz, C. A. Mirkin, *Proc. Natl. Acad. Sci. USA* **2006**, *103*, 13300.
- [70] D. M. O'Carroll, C. E. Hofmann, H. A. Atwater, *Adv. Mater.* **2010**, *22*, 1223.
- [71] M. L. Pedano, S. Li, G. C. Schatz, C. A. Mirkin, *Angew. Chem. Int. Ed.* **2010**, *49*, 78.
- [72] W. Wei, S. Z. Li, J. E. Millstone, M. J. Banholzer, X. D. Chen, X. Y. Xu, G. C. Schatz, C. A. Mirkin, *Angew. Chem. Int. Ed.* **2009**, *48*, 4210.
- [73] M. J. Banholzer, L. Qin, J. E. Millstone, K. D. Osberg, C. A. Mirkin, *Nat. Prot.* **2009**, *4*, 838.
- [74] K. D. Osberg, M. Rycenga, N. Harris, A. L. Schmucker, M. R. Langille, G. C. Schatz, C. A. Mirkin, *Nano Lett.* **2012**, *12*, 3828.
- [75] A. Gole, C. J. Murphy, *Chem. Mater.* **2005**, *17*, 1325–1330.
- [76] A. M. Alkilany, L. B. Thompson, C. J. Murphy, *ACS Appl. Mater. Interfaces* **2010**, *2*, 3417.
- [77] S. Vial, I. Pastoriza-Santos, J. Perez-Juste, L. M. Liz-Marzan, *Langmuir* **2007**, *23*, 4606.
- [78] V. Kozlovskaya, E. Khartlampieva, B. P. Khanal, P. Manna, E. R. Zubarev, V. V. Tsukruk, *Chem. Mater.* **2008**, *20*, 7474.
- [79] L. Tian, M. Fei, R. Kattumenu, A. Abbas, S. Singamaneni, *Nanotechnology* **2012**, *23*, 255502.
- [80] J. Lim, C. Lanni, E. R. Everts, F. Lanni, R. D. Tilton, S. A. Majetich, *ACS Nano* **2011**, *5*, 217.
- [81] P. K. Jain, S. Eustis, M. A. El-Sayed, *J. Phys. Chem. B* **2006**, *110*, 18243.
- [82] A. S. Stender, G. Wang, W. Sun, N. Fang, *ACS Nano* **2010**, *4*, 7667.
- [83] O. L. Muskens, G. Bachelier, N. Del Fatti, F. Vallée, A. Brioude, X. Jiang, M. P. Pileni, *J. Phys. Chem. C* **2008**, *112*, 8917.
- [84] S. Link, M. B. Mohamed, M. A. El-Sayed, *J. Phys. Chem. B* **1999**, *103*, 3073.
- [85] J.-M. Moon, A. Wei, *J. Phys. Chem. B* **2005**, *109*, 23336.
- [86] K.-S. Lee, M. A. El-Sayed, *J. Phys. Chem. B* **2005**, *109*, 20331.
- [87] S. Link, M. A. El-Sayed, *J. Phys. Chem. B* **1999**, *103*, 8410.
- [88] A. P. Li, F. Müller, A. Birner, K. Nielsch, U. Gösele, *J. Appl. Phys.* **1998**, *84*, 6023.
- [89] P. B. Johnson, R. W. Christy, *Phys. Rev. B* **1972**, *6*, 4370.
- [90] S. A. Maier, M. L. Brongersma, P. R. Kik, H. A. Atwater, *Phys. Rev. B* **2002**, *65*, 193408.
- [91] L. Slaughter, W.-S. Chang, S. Link, *J. Phys. Chem. Lett.* **2011**, *2*, 2015.

Received: January 23, 2013
Published online: March 12, 2013